Artifacts in High-Energy Compton Imaging with 3D Position Sensitive CdZnTe

Daniel Shy, Jiawei Xia, and Zhong He

***Abstract*—High-energy gamma-ray imaging is an important technique with applications in homeland security and medical imaging. Recent advancements in the Cadmium Zinc Telluride (CdZnTe) OrionUM detector systems have enabled measurement of gamma-ray sources with energies up to 9 MeV. However, Compton imaging of photons above 3 MeV faces several challenges that degrade both spectroscopic and imaging performances in pixelated CdZnTe systems. These factors include the increase in pair-production events, incorrect event sequencing, and charge sharing from large electron clouds. They all result in shift-variant image artifacts that degrade the signal-to-noise ratio as well as create artifacts that might be mistaken for a hot spot. The degradation from artifacts is analyzed, discussed, and possible mitigation techniques are presented to allow for recovery of the Compton image signal. Simulation is compared with experimental measurements of 4.4 MeV gamma rays from a ^{238}PuBe source to investigate the artifacts.**

***Index Terms*—Compton event reconstruction, gamma-ray imaging, 3-D position-sensitive CdZnTe, pair-production kinematics, high-energy gamma-ray imaging, Compton-imaging artifacts.**

I. INTRODUCTION

COMPTON imaging is a technique for estimating the directional origin of an incoming gamma-ray. It has found applications in many fields, from astronomy [1] to nuclear medicine [2]. Other implementations also exists in chemical, biological, radiological, nuclear and explosive (CBRNE) material search via gamma-ray detection [3]. High-energy gamma-ray detection, which is defined as any gamma ray above 3 MeV in this study, is used for active interrogation of special nuclear material (SNM) with the energy range of interest between 2.5 and 6 MeV [4]. Detection of high explosives also employ active interrogation with neutrons by measuring the de-excitation of nitrogen instigated by the thermal capture on the nitrogen $\{^{14}\text{N}(n,\gamma)^{15}\text{N}^*\}$ with the emission of several gamma rays ranging from 4.48 to 10.82 MeV [5]. In nuclear medicine, 4.4 and 6.1 MeV gamma rays, from the de-excitation of $^{12}\text{C}^*$ and $^{16}\text{O}^*$ respectively, are used to verify the range of the proton beam in proton therapy [2].

With 3D position sensitive detectors, such as a pixelated CdZnTe, both the position and energy deposited (E_i) of the i^{th} interaction in the sequence of the measured multi-interaction event can be recorded. This information allows for backprojection of a Compton cone to estimate the direction of the incident gamma ray, which is known as simple backprojection (SBP) imaging. The vector from the second to the first interaction location creates the "Compton axis", or "lever arm". With that, a cone is backprojected with an opening angle derived from the Compton scattering formula, and is illustrated in Fig. 1. The opening angle (Θ) between the lever arm and generatrix is represented by:

$$\cos(\Theta) = 1 - \frac{m_e c^2 E_1}{E_0(E_0 - E_1)}, \tag{1}$$

where the electron rest energy is represented by $m_e c^2$, E_1 is the deposited energy in the first interaction, and the incident energy, E_0, is either known a priori or assumed to be the summation of the observed interactions. Superimposing multiple Compton cones can reveal the estimated source location.

Compton scattering interactions, followed by a photoelectric absorption, form the basis of Compton imaging. Pair-production, however, does not preserve directional information unless the trajectory and positron of the resulting electron and positron are tracked [6], which currently cannot be accomplished with the OrionUM detector system. Therefore, events with pair production as the first interaction cannot be used for imaging.

This work explores image artifacts associated with Compton imaging of high-energy gamma rays, which can originate from either charge sharing, pair-production, or incorrectly sequenced events. Image artifacts are important to identify as they are errors in the image. They are a misrepresentation of information as they are false image structures, thereby degrading any analysis especially when no a priori knowledge is known. These artifacts can apply to other Compton imaging systems that are semiconductor or scintillator based. This manuscript also presents several techniques to mitigate some of the symptoms.

II. OVERVIEW OF TERMINOLOGY, METHODS, AND EXPERIMENTAL SETUP

A. *Terminology and Coordinate System*

An "interaction" describes a single gamma-ray interaction, while an "event" refers to a collection of interactions that originated from a single incident gamma ray. The number of "pixel events" refers to the number of anode pixels triggered in an event. Therefore, the number of pixel events may not

This work was supported by the Department of Energy NA-22 office under grant: DE-NA002131. The University of Michigan 3D CdZnTe detector development was funded under the Department of Defense DTRA award number HDTRA1-15-C-0049. Any opinions, findings and conclusions or recommendations expressed in this material are those of the authors and do not necessarily reflect the views of the U.S. Government or any agency thereof.

The authors are with the Department of Nuclear Engineering and Radiological Sciences, University of Michigan, Ann Arbor, MI 48109 USA (e-mail: shyd-at-umich.edu).

Color versions of one or more of the figures in this paper are available online at http://ieeexplore.ieee.org

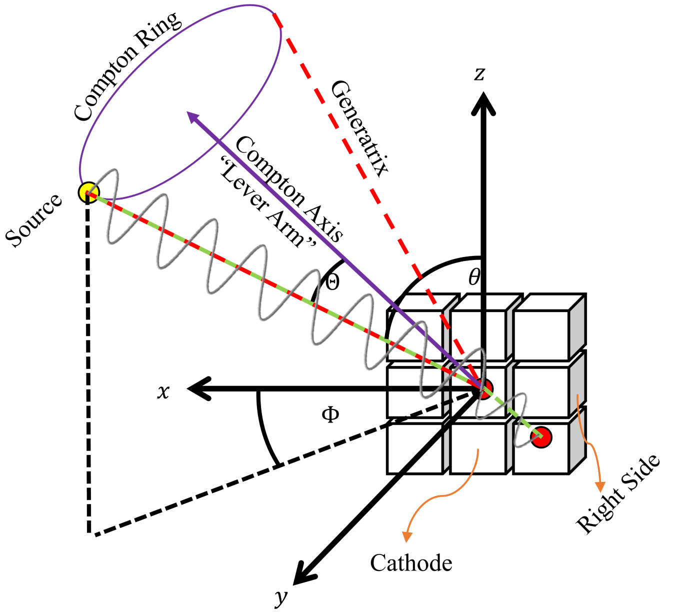

Fig. 1. Sketch of the $3 \times 3 \times 1$ OrionUM CdZnTe system where the array is placed in the $x-z$ plane. The yellow circle represents a source which emits a gamma ray (grey), then Compton scatters off the red circle and photoabsorbs in the next location. A Compton cone (red) with opening angle of Θ is backprojected onto a spherical image space which intersects it in what is known as a Compton ring (purple). The cathode plane has a normal vector of $\hat{y}$ and the anode has a normal vector of $-\hat{y}$.

match the number of interactions due to the pixelated nature of the detector. A "side-neighbouring event" refers to any event where two recorded pixel-interactions occur in adjacent pixels. This could be a result of a gamma ray that scattered into the neighbouring pixel, or a "charge sharing" event where a single interaction produced an electron cloud that is collected by multiple anode pixels.

Fig. 1 sketches the 3×3 crystal OrionUM detector with a coordinate system that is consistent throughout the manuscript. In the schematic, the normal of the cathode is in the $\hat{y}$ direction and the source is located in coordinate (ϕ, θ). Additional detail on the OrionUM system is available in Sec. II-B.

B. The University of Michigan 4π Compton Gamma-Ray Imager

This study uses the University of Michigan 4π OrionUM Compton imager [7], composed of a $3 \times 3 \times 1$ array of $2 \times 2 \times 1.5$ cm^3 CdZnTe crystals. Each crystal has an 11×11 pixelated anode array, with a 1.72 mm pixel pitch, and a planar cathode. When a pixel triggers, the position within the pixelated plane is resolved while the depth of interaction is calculated via the cathode-to-anode ratio or timing. However, if two interactions were to occur under the same pixel, the reconstruction algorithm will concatenate them to a single interaction event.

The same system was used in [8], which features the system more in depth as well as a description of the GEANT4 simulation configuration. The simulation model also took electron thermalization into consideration and the track of the electron recorded. The physics libraries implemented are pair-production, Compton Scattering, photoelectric effect, all from the Livermore low energy physics package as well as electron-matter interaction libraries [9].

Fig. 2 presents the electron cloud size as a function of deposited energy as simulated in GEANT4 by tracking the electron after a gamma-ray interaction. In this study, electron cloud diameter was defined as the largest separation between two ionized electrons produced along the thermalization of the recoiled electron [10]. The horizontal dashed blue line represents the pixel pitch. The average electron cloud size at 511 keV is about 220 μm while a 2 MeV event results in 1180 μm cloud. The energy where the electron cloud is the size of the pixel pitch is about 2.75 MeV. The mean free path of a 511 keV photon in CdZnTe is about 2.2 cm, which includes scattering and photoelectric cross section.

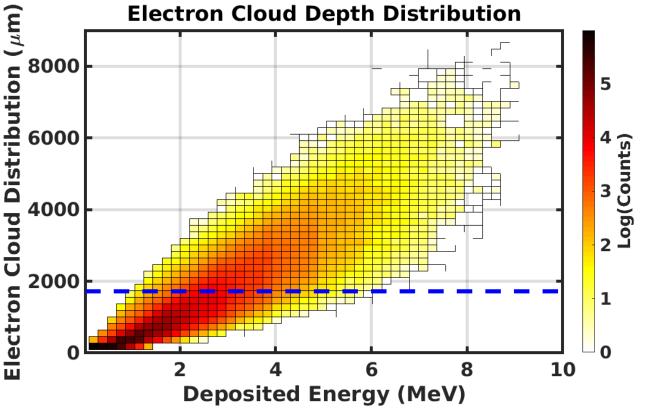

Fig. 2. Simulated electron cloud size as a function of deposited energy. The pixel pitch is represented by the horizontal dashed blue line at 1720 μm.

C. Sequence Reconstruction of Gamma-Ray Interactions

Interactions in an event must be sequenced before any image reconstruction can take place in CdZnTe, due to its poor time

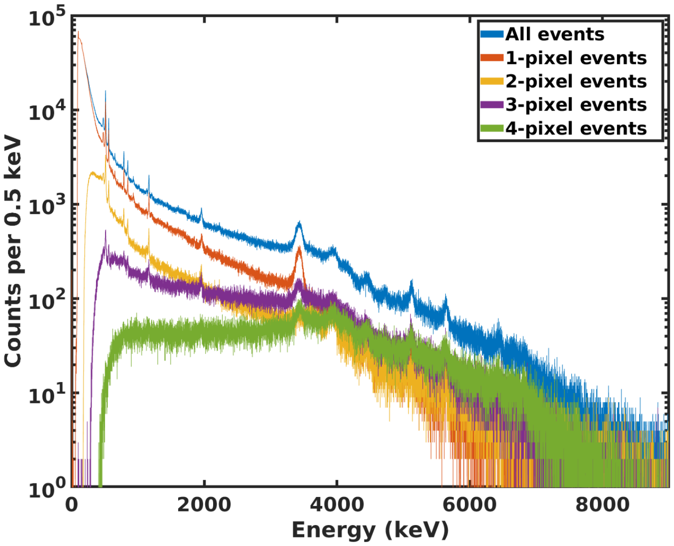

Fig. 3. Gamma-ray spectrum of a PuBe source in a PVC target for the different number of interactions. The data corresponds to the cathode irradiation discussed in Sec. II-D.

resolution. The specific sequencing algorithm implemented depends on the number of observed interactions in an event.

For two-pixel events, the applied sequencing method is known as simple comparison, which compares the energies of each interaction with the Compton edge and amongst themselves [11]. Three-or-more pixel events are sequenced with the “Mean Squared Difference” method [12][13], where each possible permutation is assigned a figure-of-merit (FOM), and the sequence with highest FOM is selected. Unless stated otherwise ‘Simple Comparison’ and ‘MSD’ are the two algorithms used in the study.

The final sequencing algorithm investigated, also for three-or-more interaction events, is “FIL-MSD” (First Is Largest), which uses the same permutation-FOM technique as MSD [8]. However, the first interaction is fixed to be the largest energy deposited interaction in the event. This algorithm proved to be more effective than MSD for energies above 1 MeV range and will be discussed in Sec. V-C as possible artifact mitigation techniques.

D. Setup and Image Artifacts in High-Energy Gamma-Ray Imaging

Fig. 3 shows a gamma-ray spectrum using the OrionUM system for a PuBe source in a polyvinyl chloride (PVC) target. The PVC was placed in order to produce higher energy gamma rays from the neutron capture on ^{35}Cl, which were not used in this study, but added noise in the image through its continuum. Two measurements were completed, one cathode irradiation and one left side irradiation where the source was placed in the $+\hat{x}$.

The artifacts associated with high-energy gamma-ray imaging are of interest as they are shift variant. In other words, the artifact locations do not shift when the source changes location and the artifact’s features, generally, do not change shape. Unless stated otherwise, measurements were done with a ^{238}PuBe source, which emits a characteristic 4.442 MeV gamma ray from an excited state of ^{12}C* from the reaction $\alpha + \text{Be} \rightarrow \text{n} + {}^{12}\text{C}^*$ [14] with an energy spectrum available in Fig. 3. Only photopeak events were considered for imaging and wide energy bounds $[4.375, 4.589]$ MeV were chosen due to the Doppler broadening of the resulting 4.4 MeV gamma ray.

Fig. 4a shows a reconstructed image of a cathode irradiation which is compromised with significant artifacts that conceals the source hotspot completely. Placing the source on the left side of the detector $(+\hat{x})$, as shown in Fig. 4b, results in a faint hotspot at $(\phi, \theta) = (0°, 90°)$, but with significant background noise and a false hotspot at $(180°, 90°)$. Regardless of the source location, the images contain a checkered artifact centered at $(270°, 90°)$, which does not shift with the source location. The major contributor to this artifact are charge sharing effects which will be discussed in Sec. IV. Additional artifacts are present along the prime and 180^{th} meridian (all locations where $\phi = 0°$ and $180°$) of the image space which arising from pair-production interaction and incorrectly sequenced events, discussed in Sec. III and IV respectively. All this analysis is done for ‘simple backprojection’ (SBP) while a discussion on its affect on advanced image reconstruction techniques is available in Sec. V-E.

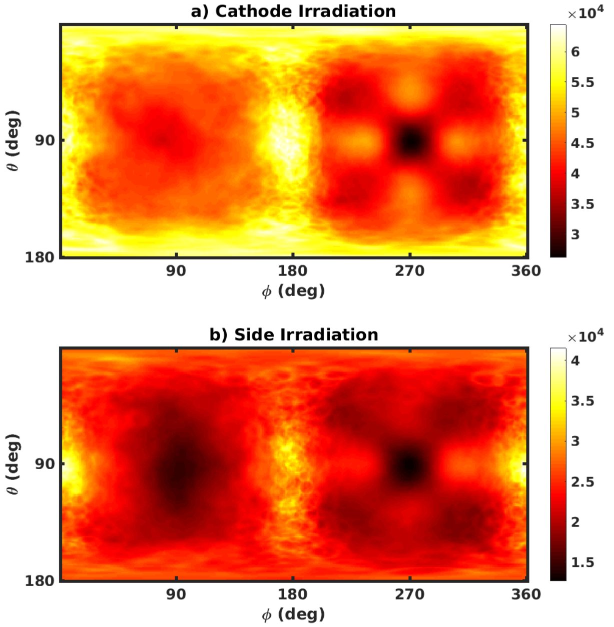

Fig. 4. Raw SBP images of a PuBe source for a) cathode irradiation with source location $(90°, 90°)$ using 33,000 imaged counts, b) left side irradiation from $(0°, 90°)$ consisting of 16,000 counts. No events were removed and the sequencing algorithms used were ‘Simple Comparison’ and ‘MSD’. The data considers 2, 3, 4, and 5 pixel events. From the two images, there appears to be significant artifacts in the prime and 180^{th} meridian of the image along with a checkered pattern located around $(270°, 90°)$. The color scale represents intensity.

III. ARTIFACTS FROM PAIR PRODUCTION EVENTS

A pair-production interaction creates an electron-positron pair where the positron will thermalize and annihilate with an electron and produce two annihilation photons at 511 keV $(e^+ + e^- \rightarrow \gamma + \gamma)$. The annihilation photons are generally emitted colinearly in anti-parallel directions. In a photopeak event, the gamma ray deposits all its energy. Therefore, under the photopeak, if the first interaction results in a pair production, both the annihilation photons must deposit their whole energies in the detector.

As this section aims to consider only pair-production artifacts, side-neighbouring events were removed from the datasets since charge sharing and pair-production event cannot be distinguished reliably. Fig. 5 plots the PuBe measurements with artifacts visible along the prime and 180^{th} meridian. This section explores this artifact and breaks it down into two components: distribution of the reconstructed Compton axes and the distribution of opening angles.

A. Distribution of Reconstructed Compton Lever Arm Axes

The distribution of reconstructed lever arms differs between pair-productions and Compton interactions. Fig. 6 plots the distribution on the image space for both types of events. Fig. 6a-b plots the distribution of a ^{137}Cs cathode irradiation

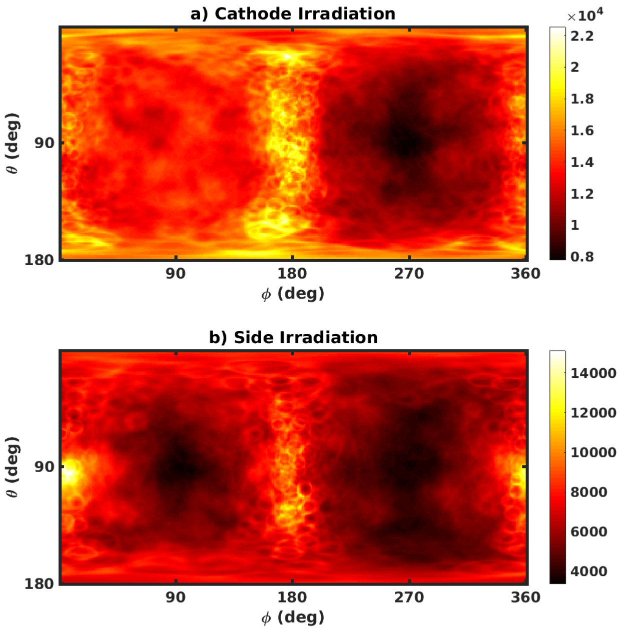

Fig. 5. SBP images without side-neighbouring events of a PuBe source placed in front of the a) cathode $(90°, 90°)$ with 9,000 counts and b) the left side $(0°, 90°)$ with 4,200 counts. Both images present severe contamination by pair-production events as observed by the small opening angle cones along the prime and 180^{th} meridian.

for simulated and experimental measurements. In an ideal infinitely large system, the distribution will follow that of the Klein–Nishina differential cross section. However, since the detector is pixelated and finite, the locations of interactions are discretized and create fixed possible lever arms.

Pair-production does not, by definition, have lever arms so the 'Compton axis' is defined as the vector between the second to the first sequenced interaction that are falsely reconstructed by the Compton imaging algorithm.

The lever arms produced by pair-production events are biased to the prime and 180^{th} meridian of the image sphere, which are associated with the sides of the detectors, away from the anode and cathode direction. Their distribution, like the artifact themselves, are independent of source location. This is shown in Fig. 6c-d which show the distribution of lever arm vectors on an image space for a simulated 4.4 MeV gamma-ray source with different irradiation locations. Although the annihilation photons have a non-uniform distribution with respect to the momentum of the positron [15], they can be considered to be emitted isotropically, (where the two photons are emitted in opposite directions), and has a nearly random walk towards the end of its track. It is therefore natural to conclude that the lever arm vectors from the events will also be isotropic in the image space. However, the system response creates a void in the space in front of the anode and cathode which is due to the pixelation of the detector. Any two interactions that occurs laterally in the y-axis will be summed into a single observed pixel or side-neighbouring event. However, if the events are separated in the $x-z$ axis, the system is then able to distinguish the different interactions.

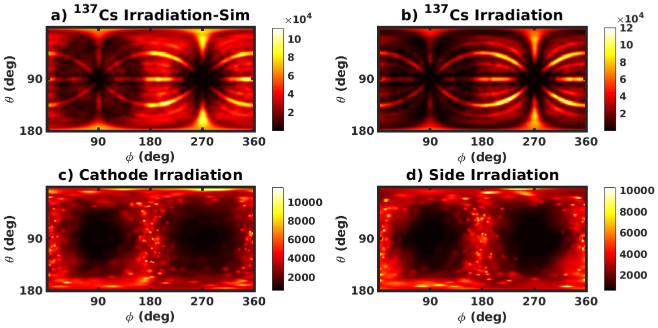

Fig. 6. Distribution of the Compton axis lever arms projected onto the image space. The top row presents cathode irradiations $(90°, 90°)$ with a) simulated ^{137}Cs source and b) an experimental ^{137}Cs irradiation, which show the expected distribution of lever arms from Compton interactions and agreement between simulation and experiment. The concentric "eyelid" bands arise from the pixelation of the detector which discretizes the distribution of lever arms. The lever arms projected onto the image space for a simulated 4.4 MeV source given that the first interaction undergoes a pair-production is presented for c) cathode irradiation $(90°, 90°)$ and d) irradiation from $(180°, 90°)$.

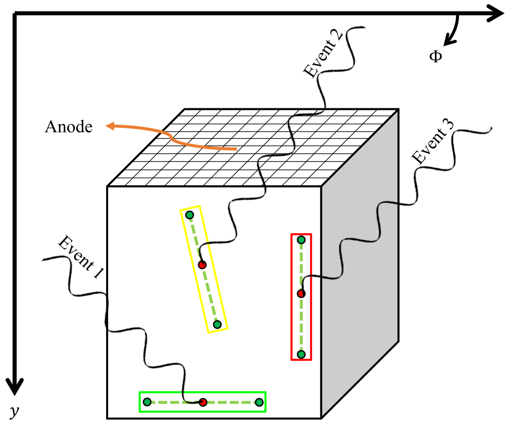

Fig. 7. Three possible events where pair-production is the first interaction with full energy deposition. Event 1 demonstrates the two annihilation photons that have been separated sufficiently to be recorded as a three-pixel event. Event 2 results in a side-neighbouring event and therefore would not produce any lever arms in the cathode/anode direction. Event 3 would result in a single pixel event as the detector would not be able to distinguish between the different depths.

Fig. 7 illustrates three possible events which aid in the understanding of the directional bias of pair-production produced lever arms. In the figure, "Event 1" shows a 3-pixel event where the resulting annihilation photons have interacted in the $x-z$ plane and have sufficient distance between them to distinguish the three separate interactions. "Event 2" results in side-neighbouring interactions which are discussed in Sec. IV. In the current section, they are removed from the data, adding to the void in the distribution. "Event 3" shows a 3 interaction event that will be concatenated into a single pixel event thereby not creating a lever arm in the anode or cathode direction.

B. Reconstructed Opening Cone Angle Distribution

The ideal distribution of Θ would resemble the Klein–Nishina differential cross section distribution. However, system geometry, asymmetry, electronic threshold, and source location all affect the distribution of detected scatter angles. In addition, incorrect event sequencing alters the distribution.

Fig. 8 plots the distribution based on the number of pixel events and interaction mechanisms. The simulated data models a 4.4 MeV gamma source where "Sim-Pair Production" only considers events when pair-production is the first interaction while "Sim-Scattering/Photoelectric" only considers events when Compton scattering or photoelectric interactions occur first. The experimental data presents the cathode irradiation with the PuBe source (same data as Fig. 5a). Finally, the "True Scattering Distribution" represents a simulated distribution of Compton scatters with true sequencing for incident 4.4 MeV gamma rays while the other simulated datasets are processed as they would for standard SBP imaging with sequencing algorithms.

Several features are observed in the angle distribution of the experimental data set, including a peak in the low angle region, $\Theta = 7^\circ, 10^\circ$, and $\sim 83^\circ$. These features contribute to image artifacts. Since there is no reliable experimental technique to differentiate between pair-production and Compton scattering, the experimental data contains both interactions and is analogous to the sum of "Sim-Pair Production" and "Sim-Compton Scattering/Photoelectric" data.

1) Two-Pixel Event Opening Angle Distribution: The large discontinuity for the sequenced two-pixel events in the Fig. 8a is a consequence of the sequencing algorithm. The nature of the simple comparison algorithm organizes the events into two regions. The two regions are characterized by energy of the first interaction (E_1): $E_1 = (0, \frac{m_e c^2 E_0}{m_e c^2 + E_0})$ and $E_1 = (0.5E_0, Compton\ Edge]$. The behaviour of the two regions are discussed in the following:

1) The first region consists of small angle scatters where the second deposited energy is larger than the Compton edge. This is when the first interaction deposits less than $E_1 = (m_e c^2 E_0)/(m_e c^2 + E_0)$, which the algorithms sequences correctly.
2) The second region is characterized when the first interaction has deposited energy greater than $0.5E_0$, which involves "large" scatters.

Therefore, if the first interaction deposits in the range $E_1 = [\frac{m_e c^2 E_0}{m_e c^2 + E_0}, 0.5E_0]$, the event will be falsely sequenced and placed into region (2) leaving a void in the distribution.

The small angle features in Fig. 8a are visible in both the experimental and the 'Sim-Scattering/Photoelectric' data. They represent events that have had bremsstrahlung or characteristic x-rays that triggered another pixel, events that have undergone charge sharing, and events that have multiple interaction under the same pixel.

Another significant feature peaks at $(\Theta \sim 83^\circ)$ and is visible in both the 'Sim-Pair Production' and experimental data, but not in the 'Sim-Scattering/Photoelectric' data. The peak is produced when one annihilation photon interacts at the same location as the pair-production event and the other interacts elsewhere in the detector. Therefore, the two recorded interactions for an incident 4.4 MeV gamma ray would be $\{0.511, 3.880\}$ MeV. The sequencing algorithm would choose the larger energy as the first interaction leading to a $\Theta \approx 83.3^\circ$.

2) Three-or-More Pixel Event Opening Angle Distribution: Three pixel events naturally occur with pair production; the creation site and the two annihilation photons. If a pair production event leads to more than three interactions, it could indicate that one of the annihilation photons Compton scattered, or that charge sharing has occurred. This section only analyzes three pixel events, but could be extrapolated into 3+ pixel events.

Due to the sensitive behaviour of the MSD algorithm and the fact that it does not account for pair-production physics, either the pair-creation site or the annihilation photon may be sequenced first. If the annihilation photon is sequenced first, the calculated opening angle for a 4.4 MeV will result in $\Theta = 10^\circ$, which is a visible artifact in Fig. 8b in the sim-pair production and experimental data. Like in the two-pixel data, there is a peak around $(\Theta \sim 83^\circ)$ due to the pair-production+annihilation photon interaction site being sequenced as the first interaction. Although not visible in the experimental data, there is a peak at $(\Theta \sim 52^\circ)$ which corresponds to when the pair-creation site is sequenced first. There are additional events with opening angles less the 10.02°, which represent incorrectly sequenced events and discussed are in Sec. IV.

C. Conclusion of Pair Production Artifacts

The artifacts observed from pair-production characteristically produce Compton cones with opening angle near 10°, 52° and 83° for an incident 4.4 MeV gamma ray. Two and three pixel events produce a cone with an opening angle of 83° for when the 511 keV interacts at the same location as the pair creation site and is then sequenced first. Three pixel events produce an opening angle of 10° when the annihilation photon is sequenced first, 52° when the pair-creation site is sequenced first. Fig. 9 illustrate the different opening angles that might occur.

The resulting image artifacts from pair-production are isolated and plotted in Fig. 10. Although low opening angles can easily be identified as background, the large opening angles can give the illusion of a hot spot, when in actuality they are superimposed rings that added constructively.

IV. ARTIFACTS OF SIDE-NEIGHBOURING, CHARGE SHARING, AND INCORRECTLY SEQUENCED EVENTS

After a Compton scatter, an electron is ejected with energy proportional to the energy deposited by the gamma ray. With an electron that has a larger initial energy, naturally, a larger "electron cloud" whose generated spatial cross section may span multiple pixels. The induced charge is then shared between multiple pixels which degrades the induced signal due to weighting potential cross-talk (WPCT) and readout electronic noise [10].

The larger electron clouds lead to worse position resolution [16]. Combined with the energy blurring effects, like Doppler broadening, the event sequencing efficiency is reduced which adds significant image artifacts.

A. Artifacts from Charge Sharing and Side-Neighbouring Events

Fig. 11 is an image reconstructed using only side-neighbouring events from the PuBe measurement. As seen in

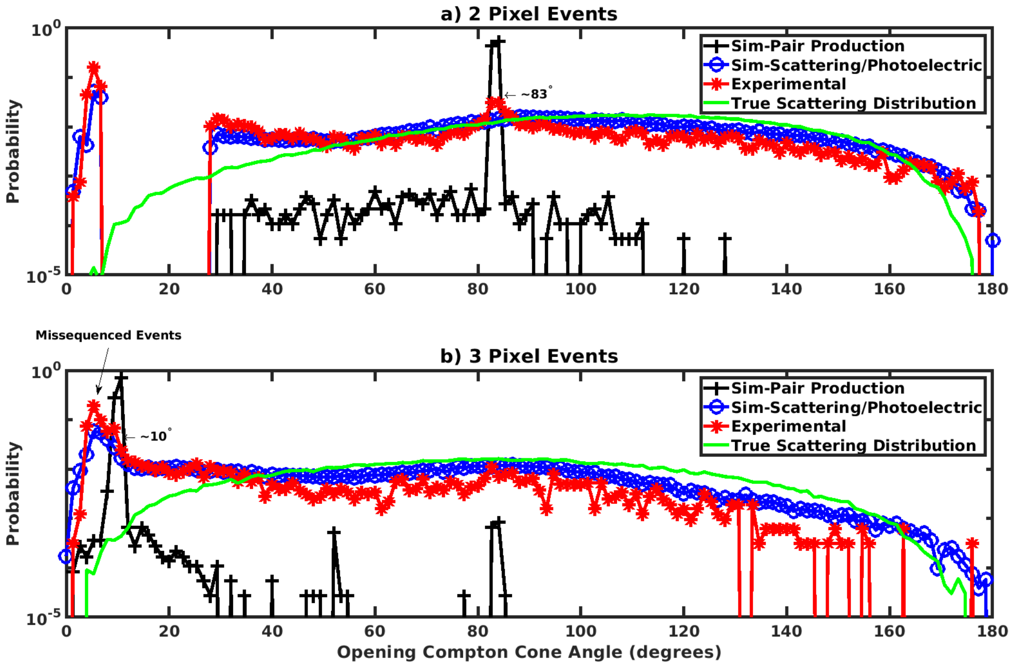

Fig. 8. Distribution of opening angles for a) two-interaction events and b) three-interaction events. The simulated data models a 4.4 MeV gamma-ray source where the ‘Sim-Pair Production’ data represents events when the first interaction results in pair-production by any other possible interaction physics while the Compton scatter/photoelectric data (blue circle) only contain Compton scattering or photoelectric effect as the first interaction. The experimental data is from the cathode irradiation with the PuBe source. ‘True Scattering Distribution’ (green solid line) represents the simulated opening angle distribution for correctly sequenced events. The red asterisk curve presents the experimental distribution.

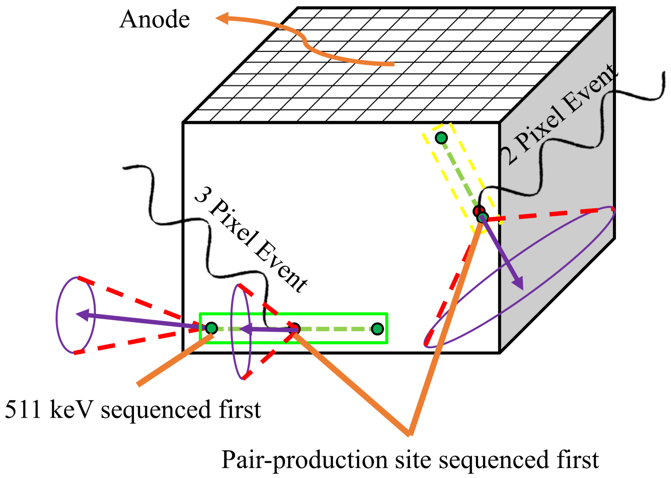

Fig. 9. A graphic presenting 3 possible reconstructed cones of pair-production events. The green circles represent the annihilation photons undergoing a photoelectric event while the red circles represent the pair-creation site. Two pixel interactions are reconstructed with an opening angle of ($\Theta \sim 83°$) for a 4.4 MeV event while a three pixel event reconstructs 10° or 50° depending on how the event is sequenced.

the image, cones are biased to the prime and 180th meridians in the image. This is largely due to the side-neighbouring events being reconstructed in the $x - z$ plane without much separation in depth ($\hat{y}$). If an electron cloud is elongated in the $\hat{y}$ direction, the detector will reconstruct a single pixel event. However, interactions that expand in the $x - z$ plane will be recorded as a multiple pixel event. Since recorded multi-pixel events are distributed in the $x - z$ plane, reconstructed lever

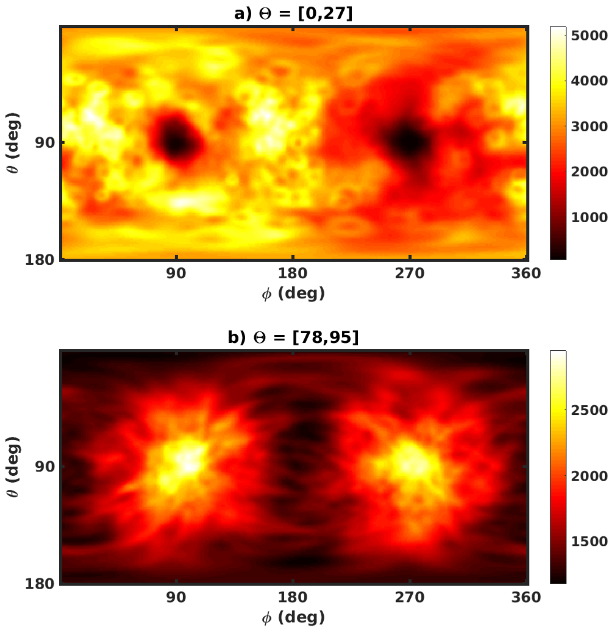

Fig. 10. Isolated artifacts due to pair-production and incorrectly sequenced events in Compton images for cones reconstructed with an opening angle range of a) $\Theta = [0, 27]°$, which represent mostly incorrectly sequenced events with some pair-production artifacts from $\Theta = 10°$. b) Is an image using only $\Theta = [78, 95]°$ which represent mostly pair-production events. Both images are from cathode irradiation and present in 2, 3, 4, and 5 pixel events.

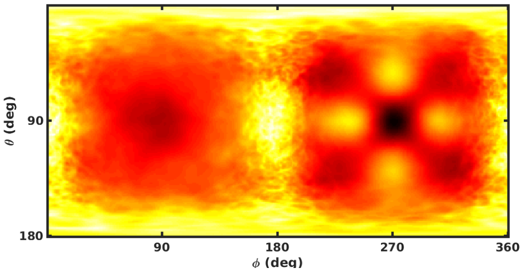

Fig. 11. Raw SBP images of a PuBe source cathode irradiation $(90°, 90°)$ using 24,000 side-neighbouring events. The sequencing algorithms used were ‘Simple Comparison’ and ‘MSD’.

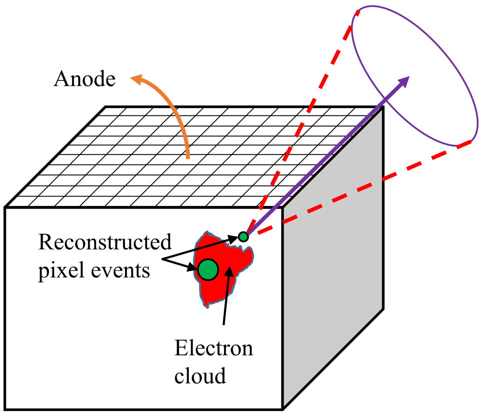

Fig. 12. Presented is an example of weighting potential cross-talk that effects the reconstruction of a two pixel event. Illustrated in red is an electron cloud that spans two pixels. The electron cloud is then reconstructed to two events shown in green. Due to WPCT, the part of the cloud that is smaller, will be reconstructed closer to the anode. Finally, a Compton cone is sketch to show the final reconstruction.

arms will be biased away from $\pm\hat{y}$.

Another charge-sharing artifact is a checkered pattern region centered at $(270°, 90°)$, a direction associated with the anode. The artifact is present in both the cathode and side irradiation and do not shift location when the source location shifts. This phenomena arises from large electron clouds that encompass multiple pixels where one pixels collects a majority of the electrons while the neighbouring pixel collects less charge. Due to WPCT, the triggered pixel that collects less of the electron cloud will reconstruct the event closer to the anode. Therefore, what is a single interaction will be recorded as a two adjacent pixel event with one of the pixel event incorrectly reconstructed as being closer to the anode. This now creates a vector in the direction of the anode, as shown in Fig. 12. A more in depth discussion on WPCT can be found in [17].

B. *Artifacts from Incorrect Event Sequencing*

Some of the artifacts from incorrectly sequenced events have been characterized for a 662 keV source in Lehner *et al.* [18]. However, in high-energy gamma rays, their mechanisms slightly differ. Referencing Eq. 1, a larger E_0 and a small E_1, which the incorrect sequence will infer, may lead to a small opening angle away from the cathode and anode direction. This can be seen in Fig. 8b, where there are a significant number of events with opening angles under $10°$, in both the experimental results and simulated data with only Compton scattering physics. In addition, the true distribution of scattering events does not show a large distribution of small angle scattering. The isolated artifacts can be seen in Fig. 10a.

V. TECHNIQUES FOR ARTIFACT MITIGATION IN HIGH-ENERGY GAMMA-RAY IMAGING

A. *Discussion of Charge Sharing Events*

Artifacts from side-neighbouring events are simple to identify as events with interactions in adjacent pixels are most likely from charge-sharing. Removing these events results in a 75% loss in counts for either the side or cathode irradiation. These events can then in principle be clustered together, as done in [19] for two pixel events, but will require further research to optimize for high-energy gamma-ray events. Thought must be given to distinguishing between charge sharing, a true side-neighbouring events (a Compton scatter followed with a photoelectric event), and pair-production events. In addition, a high threshold was chosen to reduce noise and reducing the number of low-energy events readout during measurement as the detector has low efficiencies at that energy. Therefore, if the events were to be clustered, there will be missing energy from the pixels that did not record charge beneath the threshold.

B. *Tagging of 511 keV Annihilation Photon*

Since pair-production can organically be tagged by the detection of a 511 keV interaction, it is natural to conclude that omitting events that have an energy deposition of 511 keV will remove pair-production artifacts. The energy range that is chosen to be removed must be generous as the resulting 511 keV from annihilation are Doppler broadened. This implies that the energy range chosen must be larger than the measured energy resolution of the system. Removing those energies and applying an opening angle cut, as presented in Sec. V-C are practically identical. It is advised to review the opening angle distribution (or the energies of the first interactions) to observe the scope of the 511 keV contamination.

C. *Opening Angle* (Θ) *Discrimination*

The artifacts presented in sections III-IV produce Compton cones with characteristic opening angles. The opening angles are summarized for each observed phenomena and are referenced by the different colour markers utilized in Fig. 13, which presents the reconstructed opening angle, Θ, as a function of incident energy for different sequenced events.

1) ***Red plus:*** These small opening angles are associated with three pixel events when the 511 keV interaction from pair-production is sequenced first and an opening angle $\Theta = \arccos\left(1 - \frac{[m_e c^2]^2}{E_0(E_0 - m_e c^2)}\right)$ is reconstructed. Other small opening cone artifacts are produced by incorrectly sequenced events, x-ray production and multiple interaction in the same pixel as seen in Sec. IV.
2) ***Green circle:*** Pair-production also results in opening angles near $\Theta = \arccos\left(1 - \frac{E_0 - 2m_e c^2}{2E_0}\right)$, when the pair-production site is sequenced first.

3) ***Blue asterisk:*** Two pixel events should be cut at angles corresponding to the curve which sequences the pair-production+annihilation first, or when $\Theta = \arccos\left(1 - \frac{E_0 - m_e c^2}{E_0}\right)$.
4) ***Black triangle:*** Two-pixel events with opening angles below the black curves ($\Theta = \arccos\left(1 - \frac{m_e c^2}{E_0}\right)$) can be removed as they might represent contamination from X-ray triggers, multiple interactions under the same pixel and pair-production event. This curve represents the lower threshold of the second range is which sequencing occurs (see Sec. III-B1). Detection of low angle scatters are less probable at high energies, seen in Fig. 8, as the photoabsorption cross section for those scattered gammas are severely reduced. In this study, imaging of events below the black curve resulted in a poor image with no apparent hotspot.

These cuts were applied to the PuBe measurement data and resulted in Fig. 14 and results in an additional loss of 50% of the image counts.

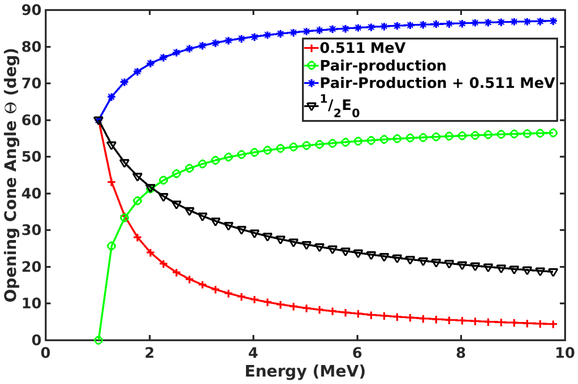

Fig. 13. Opening angles for incident energies in the range $E_0 = [1.022, 10]$ MeV and correspond to different interactions that were sequenced first. Three pixel events mostly sequences the annihilation photon first (red). The most significant two-pixel pair-production artifact results from the "Pair-production + 0.511 MeV" (in blue). Two-pixel interactions with opening angles beneath that of $\frac{1}{2}E_0$ should be discarded as they most likely correspond to charge-sharing.

D. Mitigation Through the FIL-MSD Sequencing Algorithm

Three-pixel-events can either be sequenced with MSD or FIL-MSD by the calculation of a FOM. MSD will generally sequence the 511 keV deposition to be the first interaction in pair production event. FIL-MSD will also sequence the annihilation photons first for energies below $E_0 = 3m_e c^2$, as the pair-creation site will have less energy than an annihilation photon. However, at higher energy ranges, the pair-creation site will have more deposited energy than an annihilation photon. With the pair-creation site sequenced first (by FIL-MSD), the FOM calculation results in a low or zero value as the algorithm assumes that the gamma-ray scatters off the creation site in a 90° angle, then back-scatters depositing 511 keV. A 4.4 MeV source was simulated only considering pair-production events and shows that FIL-MSD will discard ~3.5 times more pair-production events than MSD. A comparison of the two sequencing algorithms is shown in Fig. 15 using the PuBe cathode data where the FIL-MSD can produce a hotspot while the MSD algorithms still contains significant noise.

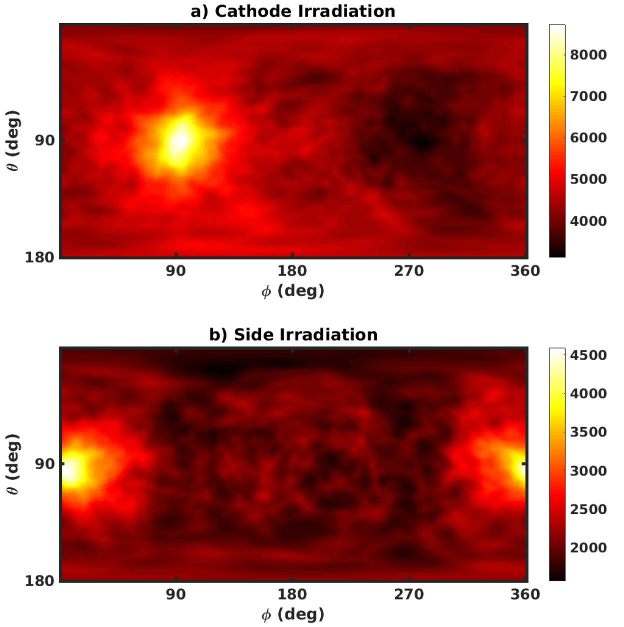

Fig. 14. SBP images of the experimental PuBe measurements with the mitigation techniques discussed in Sec.V-C. a) Presents the cathode irradiation image with 4,500 counts while b) images the side irradiation with 2,150 counts all consisting of 2, 3, 4, and 5 pixel events.

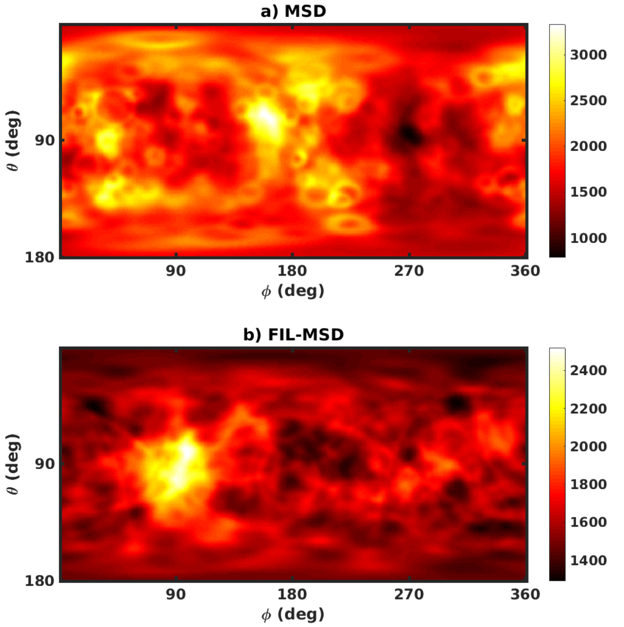

Fig. 15. PuBe measurement sequenced with a) the MSD algorithm and b) the FIL-MSD algorithm. Using the MSD algorithm, it is clear that a hotspot is not reconstructed correctly while FIL-MSD reconstructs the source. The images consist of only three-pixel events and no opening angle cuts were applied.

E. Application of Analysis to More Advanced Imaging Algorithms

The analysis on image artifacts in this study was completed using simple backprojection. However, the analysis can be quickly applied to filtered backprojection (FBP), or other inverse reconstruction techniques, since SBP imaging forms the basis to FBP. However, identifying the artifacts in iterative based image algorithms, such as maximum likelihood expected-maximization (MLEM), would not be as trivial. Additional analysis must be completed if the system response does not account for pair-production or charge sharing to understand the behaviour of such artifacts. However, event cuts could be applied during construction of the system matrix to prevent the formation of the artifacts.

VI. CONCLUSION

This work investigates the image artifacts resulting from high-energy gamma rays and characterizes them. These artifacts generally originate from charge sharing or pair-production events and can apply to other Compton imagers that are CdZnTe or scintillator based. When imaging the 4.4 MeV gamma ray from the PuBe source, pair-production contamination created artifacts with cone opening angles of 83.3° when the annihilation and pair-creation site occur under the same pixel and is sequenced first. When the annihilation photon is sequenced first, a 10° opening angle is calculated. Charge sharing and incorrectly sequenced events produce small opening cone angles which contaminate the image in the direction normal to the cathode and anode. Without using any mitigation techniques, image reconstruction was unsuccessfully, as it is not able to reconstruct the source. With this analysis, several techniques to mitigate image artifacts were presented which results in SBP images with a definitive hotspot.

ACKNOWLEDGMENTS

The authors are grateful to David Goodman and Niral Shah for valuable discussion and comments. Much appreciation is given to the anonymous referees for most valuable comments which have greatly improved the exposition of this manuscript. Many thanks to Justin Quinn for access to the various radiation sources.

REFERENCES

[1] V. Schonfelder, R. Diehl, G. G. Lichti, H. Steinle, B. N. Swanenburg, A. J. M. Deerenberg, H. Aarts, J. Lockwood, W. Webber, J. Macri, J. Ryan, G. Simpson, B. G. Taylor, K. Bennett, and M. Snelling, "The imaging compton telescope comptel on the gamma ray observatory," *IEEE Transactions on Nuclear Science*, vol. 31, no. 1, pp. 766–770, Feb 1984.

[2] E. Draeger, D. Mackin, S. Peterson, H. Chen, S. Avery, S. Beddar, and J. C. Polf, "3d prompt gamma imaging for proton beam range verification," *Physics in Medicine & Biology*, vol. 63, no. 3, p. 035019, 2018.

[3] C. Belanger-Champagne, H. Vainionpaa, P. Peura, H. Toivonen, P. Eerola, and P. Dendooven, "Design of a novel instrument for active neutron interrogation of artillery shells," *PLoS One*, vol. 12, no. 12, 12 2017.

[4] R. C. Runkle, D. L. Chichester, and S. J. Thompson, "Rattling nucleons: New developments in active interrogation of special nuclear material," *Nuclear Instruments and Methods in Physics Research Section A: Accelerators, Spectrometers, Detectors and Associated Equipment*, vol. 663, no. 1, pp. 75 – 95, 2012.

[5] G. A. de Nolfo, S. D. Hunter, L. M. Barbier, J. T. Link, S. Son, S. R. Floyd, N. Guardala, M. Skopec, and B. Stark, "Gamma-ray imaging for explosives detection," in *Chemical, Biological, Radiological, Nuclear, and Explosives (CBRNE) Sensing IX*, A. W. F. III and P. J. Gardner, Eds., vol. 6954, International Society for Optics and Photonics. SPIE, 2008, pp. 25–31. [Online]. Available: https://doi.org/10.1117/12.777176

[6] W. B. Atwood *et al.*, "The Large Area Telescope on the Fermi Gamma-ray Space Telescope Mission," *Astrophys. J.*, vol. 697, pp. 1071–1102, 2009.

[7] M. Streicher, "Applications of Digitized 3-D Position-Sensitive CdZnTe Spectrometers for National Security and Nuclear Nonproliferation," Ph.D. dissertation, University of Michigan, 2004. [Online]. Available: http://cztlab.engin.umich.edu/wp-content/uploads/sites/187/2015/03/Streicher-Thesis-May-3-2017.pdf

[8] D. Shy and Z. He, "Gamma-ray tracking for high energy gamma-ray imaging in pixelated cdznte," *Nuclear Instruments and Methods in Physics Research Section A: Accelerators, Spectrometers, Detectors and Associated Equipment*, 2018.

[9] D. Cullen, J. H. Hubbell, and L. Kissel, "Epdl97: the evaluated photo data library '97 version," 01 1997.

[10] J. C. Kim, S. E. Anderson, W. Kaye, F. Zhang, Y. Zhu, S. J. Kaye, and Z. He, "Charge sharing in common-grid pixelated cdznte detectors," *Nuclear Instruments and Methods in Physics Research Section A: Accelerators, Spectrometers, Detectors and Associated Equipment*, vol. 654, no. 1, pp. 233 – 243, 2011.

[11] D. Xu, "Gamma-ray imaging and polarization measure using 3-d position-sensitive CdZnTe detectors," Ph.D. dissertation, University of Michigan, 2006. [Online]. Available: https://cztlab.engin.umich.edu/wp-content/uploads/sites/187/2015/03/20060907-thesis.pdf

[12] C. E. Lehner, "4-pi Compton imaging using a single 3-d position sensitive CdZnTe detector," Ph.D. dissertation, University of Michigan, 2004. [Online]. Available: https://cztlab.engin.umich.edu/wp-content/uploads/sites/187/2015/03/Carolyns-Diss4-Pi-Compton-Imaging.pdf

[13] C. Wahl, "Imaging, Detection, and Identification Algorithms for Position-Sensitive Gamma-Ray Detectors," Ph.D. dissertation, University of Michigan, 2011. [Online]. Available: https://cztlab.engin.umich.edu/wp-content/uploads/sites/187/2015/03/Wahl-Thesis.pdf

[14] J. Kelley, J. Purcell, and C. Sheu, "Energy levels of light nuclei a=12," *Nuclear Physics A*, vol. 968, pp. 71 – 253, 2017.

[15] F. Berends and R. Kleiss, "Distributions for electron-positron annihilation into two and three photons," *Nuclear Physics B*, vol. 186, no. 1, pp. 22 – 34, 1981.

[16] Y. Zhu, S. E. Anderson, and Z. He, "Sub-pixel position sensing for pixelated, 3-d position sensitive, wide band-gap, semiconductor, gamma-ray detectors," *IEEE Transactions on Nuclear Science*, vol. 58, no. 3, pp. 1400–1409, June 2011.

[17] W. R. Kaye, "Energy and Position Reconstruction in Pixelated CdZnTe Detectors," Ph.D. dissertation, University of Michigan, 2012. [Online]. Available: https://cztlab.engin.umich.edu/wp-content/uploads/sites/187/2015/03/Willy-Kaye.pdf

[18] C. E. Lehner and Z. He, "Image artifacts resulting from gamma-ray tracking algorithms used with compton imagers," in *IEEE Symposium Conference Record Nuclear Science 2004.*, vol. 3, Oct 2004, pp. 1599–1603 Vol. 3.

[19] W. Wang, W. R. Kaye, J. C. Kim, F. Zhang, and Z. He, "Improvement of compton imaging efficiency by using side-neighbor events," *Nuclear Instruments and Methods in Physics Research Section A: Accelerators, Spectrometers, Detectors and Associated Equipment*, vol. 687, pp. 62 – 68, 2012.